Acta Cryst. (1982). A**38**, 753–761

Structural Studies on *A*-Cation-Deficient Perovskite-Related Phases. II. Microdomain Formation in $ThNb_4O_{12}$

BY M. LABEAU

Institut National Polytechnique de Grenoble, Laboratoire de Genie Physique, BP 46, 38402 *St Martin d'Hères, France*

I. E. GREY,* J. C. JOUBERT AND H. VINCENT

Laboratoire de Cristallographie, CNRS, 166 *X,* 38042 *Grenoble CEDEX, France*

AND M. A. ALARIO-FRANCO

Instituto de Quimica Inorganica, CSIC, Madrid, Spain

(*Received* 10 *July* 1981; *accepted* 27 *May* 1982)

Abstract

Electron diffraction/microscopy and X-ray diffraction techniques have been used to study the thorium/vacancy ordering and microdomain structures of quenched and slow-cooled samples of the *A*-cation-deficient perovskite-related phase $ThNb_4O_{12}$. In both types of samples, there is primary ordering of thorium atoms into the cuboctahedral sites in alternate $(001)_p$ layers. The quenched and slow-cooled samples have different secondary orderings of thorium atoms and vacancies in the occupied $(001)_p$ layers. In the quenched samples, the thorium atoms and vacancies are ordered in alternate rows parallel to $[100]_p$ and $[010]_p$. Short segments (20–50 Å) of the two orientation variants are statistically distributed in a type of tweed pattern, separated by boundaries that are aligned predominantly parallel to $(110)_p$ and $(\bar{1}10)_p$. In the slow-cooled samples, the ordering of columns of thorium atoms and vacancies parallel to $[110]_p$ or $[\bar{1}10]_p$ occurs in microdomains, with domain boundaries parallel to $(100)_p$ and $(010)_p$ and with average separations of $6a_p$, $6b_p \equiv 24$ Å. The domains corresponding to the two orientations of thorium columns form a checkerboard pattern of two interpenetrating sets of corner-shared squares. In either set, the ordering of columns is propagated along diagonal rows of corner-shared domains, but there is no correlation between adjacent rows. The NbO_6 octahedra are tilted about the $[110]_p$ and $[\bar{1}10]_p$ axes, parallel to the thorium-column orientations, and the domain boundaries act as mirror-twin planes for the octahedral tilt systems. This periodic change in the tilt-axis orientation gives rise to characteristic clusters of split superlattice spots in the diffraction patterns for $ThNb_4O_{12}$. Optical transform methods were used to check the validity of microdomain models for both the quenched and the slow-cooled samples.

Introduction

In part I (Alario-Franco, Grey, Joubert, Vincent & Labeau, 1982), we presented electron and X-ray diffraction results for samples of the *A*-cation-deficient perovskite-related phase $Th_{0.25}NbO_3$ (*i.e.* $ThNb_4O_{12}$), which were slowly cooled from the melt. The diffraction patterns showed both strong, sharp reflections and groups of very weak, diffuse satellite reflections. The sharp reflections, which indexed with a tetragonal perovskite supercell ($a_t = a_p$, $c_t = 2c_p$), resulted from long-range ordering of thorium atoms into alternate $(001)_p$ layers of cuboctahedral *A*-cation sites, as originally reported by Trunov & Kovba (1966). The diffuse satellite reflections were interpreted as resulting from short-range ordering of thorium atoms and vacancies within the $(001)_p$ layers. Splitting of certain groups of satellite reflections was observed, characteristic of a periodic two-dimensional array of domains, with domain boundaries oriented parallel to $(100)_p$ and $(010)_p$. However, in order to simplify the interpretation of the diffraction patterns, we considered in part I the diffraction effects arising from one type of domain only. We thus established a model for the local ordering of thorium atoms, together with associated niobium displacements and tilting of the octahedral framework, in a single-domain approximation. In this paper, we consider the nature of the microdomains and the interdomain modifications of thorium/vacancy ordering and octahedral tilts.

* Permanent address: CSIRO Division of Mineral Chemistry, PO Box 124, Port Melbourne, Victoria 3207, Australia.

0567-7394/82/060753-09$01.00

Table 1. *Summary of diffraction data for* $ThNb_4O_{12}$

	Quenched samples			
	(*a*)*	(*b*)	(*c*)	Slow-cooled sample (*d*)
Subcell parameters (Å)				
a_p, b_p	3·9010 (9)	3.8976	3·8959	3·898 (2)
c_p	3·914 (1)	3·9201 (3)	3·9223 (4)	3·926 (2)
c_p/a_p	1·003	1·005	1·006	1·007
Superlattice		$2a_p \times 2b_p \times 2c_p$		$3\sqrt{2}a_p \times \sqrt{2}b_p \times 4c_p$
Diffraction results				
1. $[010]_p$ zone $(h/2\ 0\ l/2)_p$ superlattice reflections		Sharp for *h* even Diffuse for *h* odd		Sharp for *h* even Absent for *h* odd
2. [001] zone $[h/2\ k/2\ 0]_p$ superlattice reflections	(*a*) Diffuse for *h* or *k* odd Very weak, diffuse for *h* and *k* both odd	(*b*) and (*c*) Sharp for *h* or *k* odd Split into four satellites in form of cross for *h* and *k* odd		Absent for *h* or *k* odd Split into four satellites for *h* and *k* both odd
3. Other diffuse diffraction effects		Absent		Diffuse rods elongated along $g\{110\}_p$, see Alario-Franco *et al.* (1982).

* (*a*) Quenched in an ice-cooled platinum dish from above the melting point. (*b*) Quenched in ice water from just below the melting point. (*c*) Cooled rapidly in air from just below the melting point. (*d*) Slowly cooled in furnace from 1523 K to room temperature.

We also report electron diffraction/microscopy and X-ray diffraction studies on samples of $ThNb_4O_{12}$ quenched rapidly from temperatures near the melting point. A similar microdomain texture is found in the quenched phase, but the thorium/vacancy ordering is quite different from that found in the slow-cooled phase. The results for the quenched phase give some insight into the way in which thorium ordering occurs in the slow-cooled phase, and a mechanism is proposed for the evolution of ordering with decreasing temperature.

Experimental

The experimental procedures and preparation of the slow-cooled phase are given in part I. For the preparation of the quenched phase, a mixture of Nb_2O_5 and ThO_2 was melted and held at about 30 K above its melting point (1661 K) for 15 h. The material was then cooled at 7 K h^{-1} to a few degrees below the melting point, and finally quenched in ice-water. In subsequent electron diffraction studies, this phase exhibited some diffuse reflections resulting from the onset of the ordering found in the slow-cooled phase. Hence an alternative quenching approach was tried in which a hole was drilled in a pre-reacted pellet of $ThNb_4O_{12}$ and the pellet hung on a fine platinum wire. The pellet was then placed in a vertical furnace, the temperature of which rapidly increased to above the melting point of the compound. As soon as the pellet melted, it fell from the wire into an ice-cooled platinum dish below. A small part of the product consisted of tiny spheres, and these were used in the subsequent studies in preference to the larger lumps forming the bulk of the product, which would have cooled more slowly.

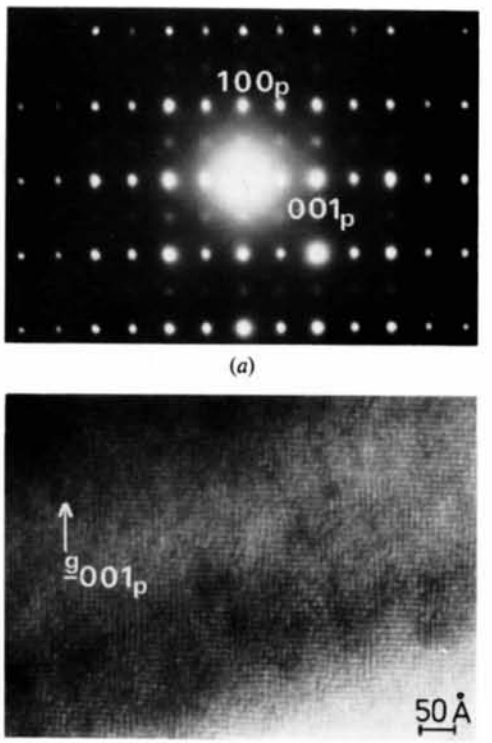

(*a*)

(*b*)

Fig. 1. Quenched $ThNb_4O_{12}$: (*a*) $[010]_p$ zone diffraction pattern; (*b*) the corresponding bright-field image.

Observations

Electron diffraction/microscopy studies

We have previously presented electron diffraction and microscopy results for slow-cooled $ThNb_4O_{12}$ (Alario-Franco *et al.*, 1982). The results obtained for quenched samples are illustrated in Figs. 1–3 and the diffraction observations for both types of sample are summarized in Table 1.

A $[010]_p$ diffraction pattern (DP), shown in Fig. 1(*a*), displays extra reflections that require a doubling of both a_p and c_p, in contrast to the slow-cooled phase in which a doubling of c_p only was observed (Alario-Franco *et al.*, 1982). The superlattice reflections along $g(100)_p$ are considerably weaker and more diffuse than those along $g(001)_p$. A bright-field image corresponding to the DP in Fig. 1(*a*) is shown in Fig. 1(*b*). It shows a patchwork-quilt array comprising segments in which 8 Å fringes parallel to $[001]_p$ are joined to other segments in which the 8 Å fringes are parallel to $[100]_p$. In some areas the fringes are replaced by an 8 Å square array of white blobs. There appears to be an antiphase arrangement of spots across some of the boundaries separating the segments, but the boundaries are indistinct and in many cases the $[100]_p$ and $[001]_p$ fringes form undulating waves with an amplitude of about 4 Å and a period of 50–100 Å.

A series of $[001]_p$ zone DPs corresponding to different quenched samples is shown in Figs. 2(*a*)–(*c*). They display extra reflections that require a doubling of both the a_p and the b_p perovskite subcell axes. In Fig. 2(*a*), corresponding to the most rapidly quenched sample, the superlattice reflections of the type $(\frac{h}{2},k,0)_p$, h odd, and $(h,\frac{k}{2},0)_p$, k odd, are broad and diffuse, and a series of even more diffuse spots can be seen at positions $(\frac{h}{2},\frac{k}{2},0)_p$, h,k odd. For samples that were quenched less rapidly, the former type of superlattice reflections are sharp and well defined, and the spots

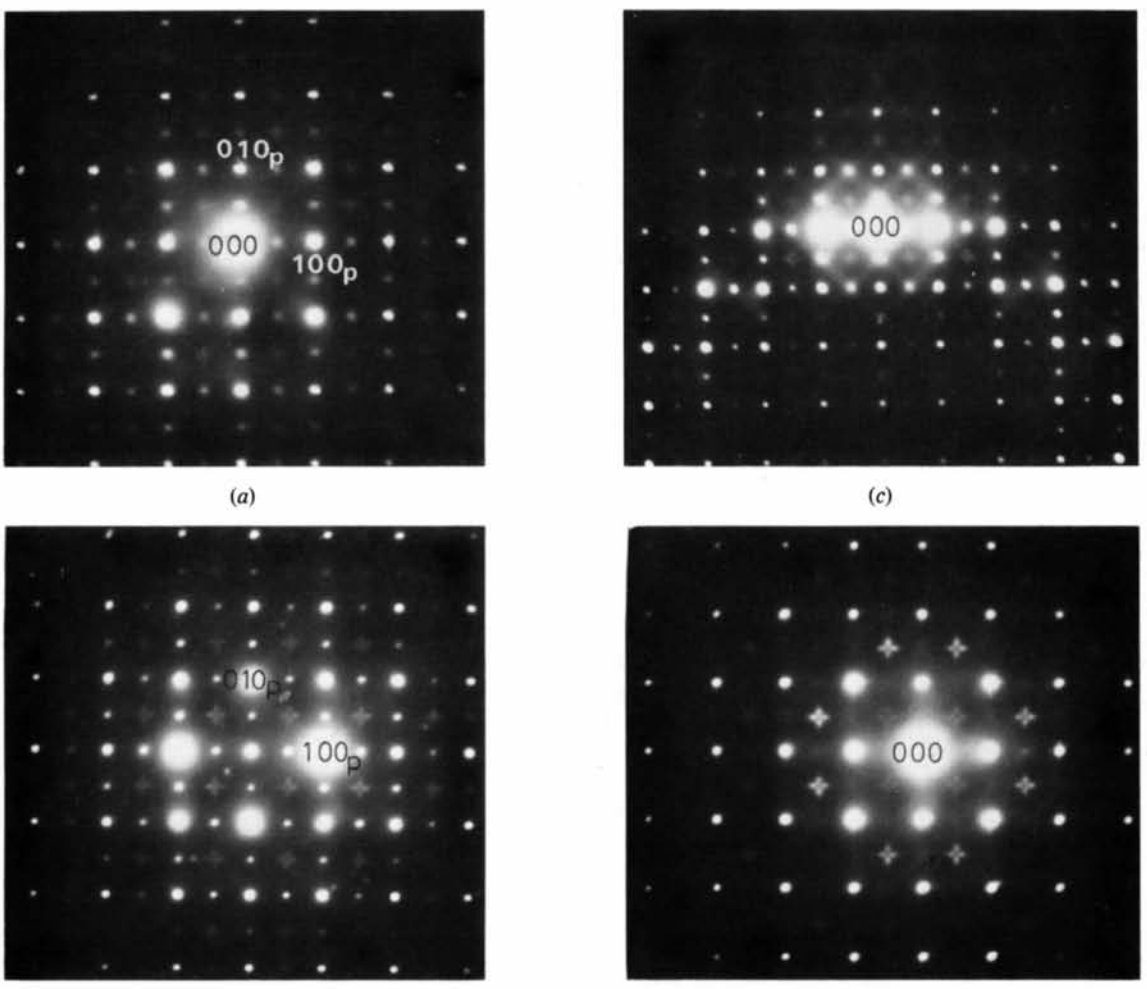

Fig. 2. $[001]_p$ zone diffraction patterns for (*a*) rapidly quenched $ThNb_4O_{12}$ (sample *a* in Table 1); (*b*) less rapidly quenched $ThNb_4O_{12}$ (sample *b* in Table 1); (*c*) as for (*b*) but tilted slightly about $g(100)_p$; (*d*) slow-cooled $ThNb_4O_{12}$.

corresponding to the latter type are replaced by clusters of four satellite reflections in the form of crosses, whose arms are parallel to $g(100)_p$ and $g(010)_p$ (Fig. 2*b*). It can be seen that the satellites are actually rod-like, being elongated in the direction corresponding to the splitting. The splitting of the satellites corresponds to periodicities close to $6 \times a_p$ and $6 \times b_p$. Slight tilting of $[001]_p$ zone DPs about $g(100)_p$ or $g(010)_p$ revealed weak diffuse streaks, parallel to $g(110)_p$ and $g(\bar{1}10)_p$, that intersected the superlattice reflections of the type $(\frac{h}{2},k,0)_p$, h odd, and $(h,\frac{k}{2},0)_p$, k odd (Fig. 2*c*).

A bright-field image taken from a $[001]_p$ zone DP is shown in Fig. 3(*a*). It comprises a complex interpenetrating system of short (<50 Å) 8 Å fringes parallel to $[100]_p$ and $[010]_p$. A 4 Å spacing of white spots is (poorly) resolved along the fringes in some areas. The fringes are rarely straight; they display the same undulations observed in the $[010]_p$ zone-axis image (Fig. 1*b*). Short $[100]_p$ and $[010]_p$ segments of fringes join to form maze-like patterns. The quasi-periodic patchwork-like domain structure in Fig. 1(*b*) is not evident in images from $[001]_p$ zone DPs. The image shown in Fig. 3(*b*) is also taken from a $[001]_p$ zone DP. In this case, the 4 Å spacing between the white spots along the 8 Å fringes is clearly resolved. Only one orientation of fringes can be seen in this image.

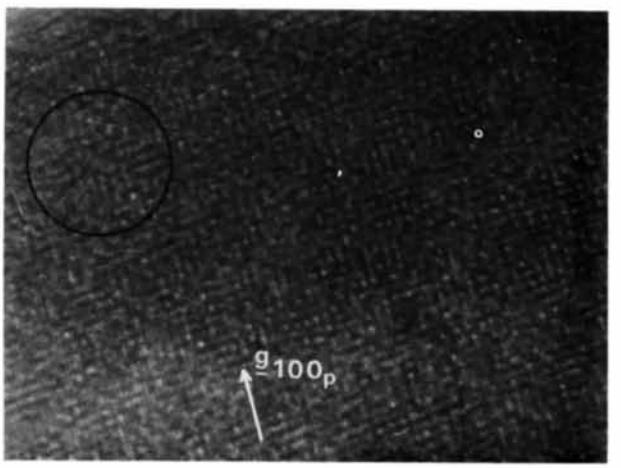

(*a*)

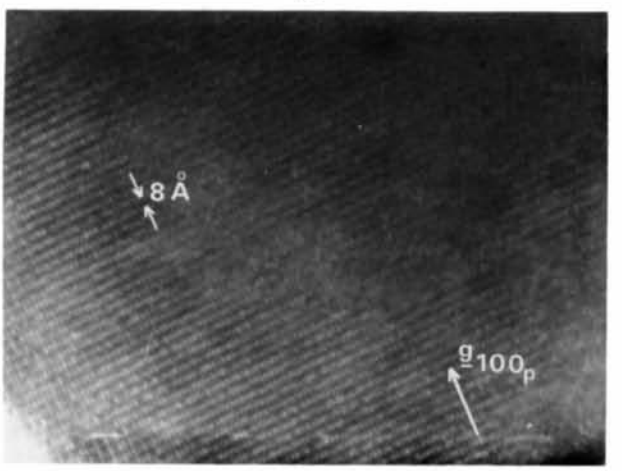

(*b*)

Fig. 3. Bright-field images obtained from $[001]_p$ zone diffraction patterns for quenched $ThNb_4O_{12}$.

In Fig. 2(*d*) a $[001]_p$ zone DP for slow-cooled $ThNb_4O_{12}$ is reproduced for comparison with the quenched samples. The superlattic reflections of the type $(h,\frac{k}{2},0)_p$, k odd, and $(\frac{h}{2},k,0)_p$, h odd, are absent for the slow-cooled specimens. However, the crosses of four satellites at $(\frac{h}{2},\frac{k}{2},0)_p$, h,k odd, remain, and they are generally sharper and more clearly resolved than they are for the quenched samples. The separation of the satellites corresponds to periodicities close to $6 \times a_p$ and $6 \times b_p$ respectively, as for the quenched samples.

X-ray diffraction studies

Quenched $ThNb_4O_{12}$. Lattice parameters for the $ThNb_4O_{12}$ samples subjected to different quenching conditions are given in Table 1, along with similar parameters for the slow-cooled phase. A correlation is apparent between the rate of quenching and the c_p/a_p ratio; the more rapid the quenching, the closer c_p/a_p is to 1·000. Even for the sample subjected to the most rapid quenching directly from the melt, the Guinier powder patterns displayed quite sharp reflections corresponding to a tetragonal subcell; *i.e.* $a_p \times b_p \times 2c_p$. These were underlain by very broad peaks corresponding to doubling of the a_p (and b_p) axes. Measurements of the half-widths of the broad peaks gave a correlation length of about 35 Å perpendicular to the $(100)_p$ and $(010)_p$ planes.

Precession photographs displayed superlattice spots at $(\frac{h}{2},0,0)_p$, $(0,\frac{k}{2},0)_p$ and $(0,0,\frac{l}{2})_p$, h,k,l odd; *i.e.* at positions requiring a doubling of all three perovskite unit-cell parameters. No intensity was observed at $(\frac{h}{2},\frac{k}{2},0)_p$, h,k odd, as occurs for $ThTa_4O_{12}$, for which a doubling of a_p and b_p has been reported by Kovba & Trunov (1962).

Slow-cooled $ThNb_4O_{12}$. The main results for the slow-cooled phase are reported in part I. Fig. 4 is an $(h,k,\frac{1}{2})_p$ precession photograph that exhibits crosses of split satellite reflections centred at $(\frac{h}{2},\frac{k}{2},\frac{1}{2})_p$, h,k odd. Note that the complete crosses are confined to positions $\{\frac{h}{2},\frac{h}{2},\frac{1}{2}\}_p$. For reflections with $h \neq k$, only one pair of satellites, corresponding to one arm of the crosses, can be seen. The satellite splitting is $\frac{1}{6} \times d^*(100)_p$ and so the corresponding average width of the domains giving rise to the crosses is $6 \times a_p$, as found also from measurements of electron DPs.

In neither the slow-cooled nor the quenched samples were crosses of split superlattice reflections observed in $(h,k,0)_p$ precession photographs, even after exposure times of up to 700 h. This is in contrast to the electron diffraction observations (Fig. 2).

Structural models

Domain structures in quenched $ThNb_4O_{12}$

Sharp $(0,0,\frac{l}{2})_p$, l odd, reflections were observed in both the X-ray and the electron DPs for all of the quenched samples, including those subjected to the most rapid quenching conditions. Furthermore, a tetragonal distortion was always evident, with $c_p/a_p > 1$ (Table 1). These observations are consistent with an ordering of thorium atoms into alternate $(001)_p$ layers of cuboctahedral sites of the perovskite structure, as discussed by Trunov & Kovba (1966); *i.e.* along c_p layers of cuboctahedra that are statistically half-filled with thorium atoms alternate with layers of empty cuboctahedra. The question to be answered is how the thorium atoms are distributed in the half-filled $(001)_p$ layers. The electron images shown in Fig. 3 suggest a model that is illustrated in Fig. 5, where $[100]_p$ rows of filled cuboctahedral sites alternate with empty rows in alternate $(001)_p$ layers. This model gives rise to $(h,\frac{k}{2},0)_p$, k odd, superlattice reflections but not to $(\frac{h}{2},\frac{k}{2},0)_p$, h,k odd, reflections. To explain the observation of both $(\frac{h}{2},k,0)_p$ and $(h,\frac{k}{2},0)_p$ reflections, it is necessary to consider a domain model with ordering of $[100]_p$ and $[010]_p$ rows of thorium atoms respectively with rows of vacancies in different domains.

Structure-factor calculations were carried out for domain models containing the two orientations of thorium-atom chains and having various domain boundaries. Two extreme examples are illustrated in Fig. 6. In Fig. 6(*a*) the domain boundaries are very regular and are parallel to $(100)_p$ and $(010)_p$, while in Fig. 6(*b*) the boundaries are irregular and are generally parallel to $(110)_p$ and $(\bar{1}10)_p$.

Irrespective of the orientation of the domain boundaries, the main changes to the perovskite DPs are the appearance of superlattice reflections at $(\frac{h}{2},k,0)_p$, h odd, and $(h,\frac{k}{2},0)_p$, k odd, as shown in Figs. 6(*c*) and (*d*). In addition to these relatively strong sharp superlattice spots, bands of weak diffuse scattering appear, connecting the superlattice spots. The diffuse bands are directly related to the orientation of the domain boundaries. For the model shown in Fig. 6(*b*), the diffuse bands are parallel to $g(110)_p$ and $g(\bar{1}10)_p$, as experimentally observed, Fig. 2(*c*), suggesting that the $[100]_p$ and $[010]_p$ chains are related across diagonal boundaries similar to those in Fig. 6(*b*). Evidence favouring this type of model is suggested by the circled area in Fig. 3(*a*), but interpreting this image in terms of

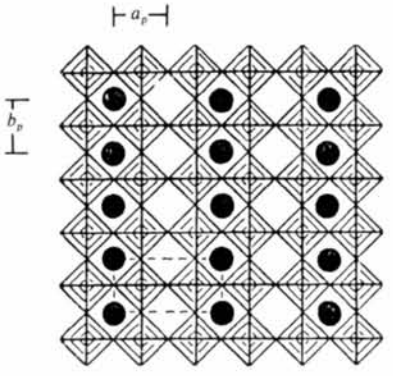

Fig. 5. Model for *A*-cation/vacancy ordering in the half-filled $(001)_p$ layers in quenched $ThNb_4O_{12}$.

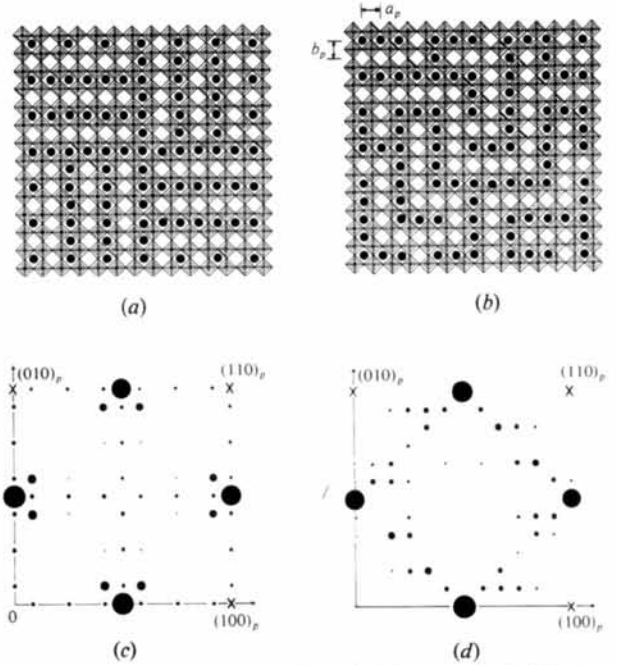

Fig. 6. Two possible microdomain models for quenched $ThNb_4O_{12}$, with domain boundaries (*a*) parallel to $(100)_p$ and $(010)_p$ and (*b*) parallel to $(110)_p$ and $(\bar{1}10)_p$. The structures are viewed in projection along $[001]_p$, and the thorium atoms are represented by the filled circles. The corresponding calculated $(h,k,l)_p$ diffraction patterns are given in (*c*) and (*d*). Subcell reflections are marked with crosses.

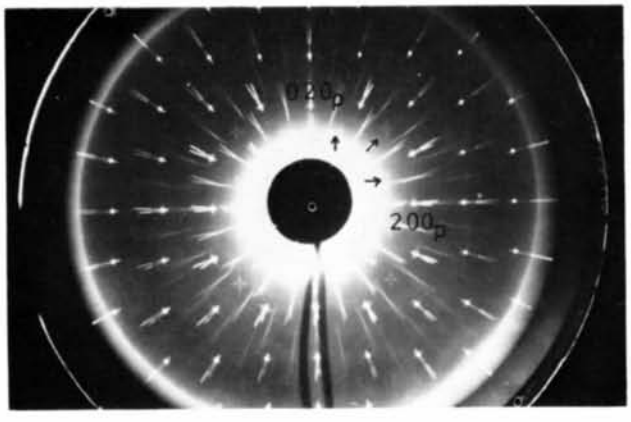

Fig. 4. Slow-cooled $ThNb_4O_{12}$: $(h,k,\frac{1}{2})_p$ precession photograph.

the projected thorium charge density is tenuous in such a disordered system, where the layers of thorium atoms perpendicular to the projection axis are not fully correlated.

Microdomain structures in slow-cooled $ThNb_4O_{12}$

Interpretation of satellite splitting in crosses. The development of split crosses of satellites at $(\frac{h}{2},\frac{k}{2},0)_p$ is illustrated in Fig. 2. For the most rapidly quenched samples, no splitting was observed (Fig. 2*a*). In contrast, splitting in the slow-cooled samples was well defined in electron DPs (Fig. 2*d*). The satellite intensities were extremely weak since they were not observed in X-ray DPs, even after exposures of many hundreds of hours. However, the crosses were easily observed in precession photographs for upper-level $[001]_p$ zone-axis DPs at positions $(\frac{h}{2},\frac{k}{2},\frac{l}{2})_p$, *h,k,l* odd; *e.g.* as shown in Fig. 4. The intensities (but not the splitting) of these reflections can be reproduced by a model comprising a system of octahedral tilts about the $[110]_p$ or $[\bar{1}10]_p$ axes together with small accompanying displacements of thorium atoms perpendicular to the tilt axes (Alario-Franco *et al.*, 1982). To explain the splitting of the satellites it is necessary to consider how this single-domain model is modified by the incorporation of quasiperiodic microdomain boundaries parallel to $(100)_p$ and $(010)_p$ with average separations of $6 \times a_p$, $6 \times b_p \simeq 24$ Å.

Using optical transform methods (Lipson, 1972), we found that the observed distribution and splitting of crosses could be qualitatively reproduced (in projection along $[001]_p$) by a regular microdomain model in which the system of octahedral tilts was reflected across periodic, intersecting $(100)_p$ and $(010)_p$ domain boundaries. The optical mask corresponding to this model is illustrated in Fig. 7(*a*), and the resulting DP is shown in Fig. 7(*b*) (compare the experimental pattern in Fig. 4). It can be seen that the domain boundaries act as mirror-twin planes for the octahedral tilt systems, and the tilt axes are alternatively parallel to $[110]_p$ and $[\bar{1}10]_p$ in adjacent domains. Perfect coherence of the oxygen framework is maintained across the boundaries. We have not attempted to account for the accompanying small displacements (~0·06 Å) of thorium atoms in the optical simulation experiments; it is apparent that the change in the orientation of the octahedral tilts alone accounts qualitatively for the main features of the observed DPs.

Inclusion of thorium/vacancy ordering. A complete microdomain model for slow-cooled $ThNb_4O_{12}$ must also explain the observed diffraction effects associated with thorium/vacancy ordering. As reported in part I, the ordering of thorium atoms and vacancies in columns parallel to $[\bar{1}10]_p$ gives rise to superlattice reflections in the form of diffuse rods elongated parallel to $g(\bar{1}10)_p$. A second set of diffuse rods, elongated parallel to $g(110)_p$, is always observed in the DPs and can be considered to arise from $[110]_p$ columns of thorium atoms and vacancies from a second type of domain. The lengths of the diffuse rods correspond to correlation lengths of 20–30 Å between $\{110\}_p$ planes of ordered thorium atoms and vacancies; *i.e.* the correlation lengths have the same magnitude as the separation between the microdomain boundaries which suggests a lack of correlation between the thorium ordering in successive domains. On the other hand, the microdomain model must allow for long-range inter-domain ordering *within* the $\{110\}_p$ planes, consistent with the relatively small cross sections of the diffuse rods (corresponding to correlation lengths of 200–300 Å).

Optical transform methods were again used to test different microdomain models for $ThNb_4O_{12}$. The most satisfactory comparison with the observed DPs (in

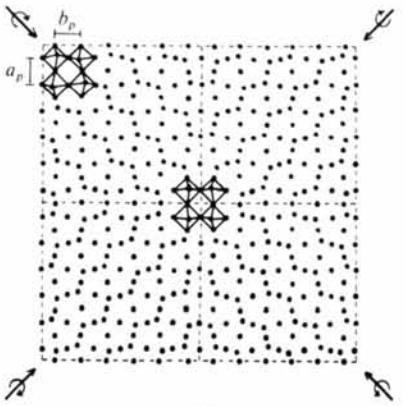

(*a*)

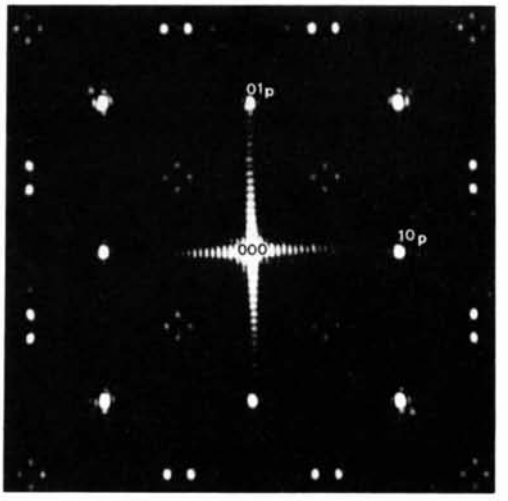

(*b*)

Fig. 7. (*a*) Part of the optical diffraction screen used to simulate octahedral tilts in a microdomain model for slow-cooled $ThNb_4O_{12}$. For clarity, the octahedra are outlined in the central section, and dashed lines have been added to indicate the domain boundaries. (*b*) The corresponding diffraction pattern, obtained by optical transform methods.

projection down $[001]_p$) was obtained by using the mask shown in Fig. 8(*a*) for the thorium/vacancy ordering. An idealized network of intersecting $(100)_p$ and $(010)_p$ domain boundaries with constant separations of $6 \times a_p$ and $6 \times b_p$ was used. The intradomain ordering was idealized as three filled $[110]_p$ (or $[\bar{1}10]_p$) rows of thorium atoms alternating with three empty rows. [The ordering actually observed is not so well developed and can be approximated by a sinusoidal modulation model (Alario-Franco *et al.*, 1982).] In the microdomain model, the periodicity perpendicular to the columns was $6 \times d(110)_p$, and it was maintained over the whole mask for each diagonal row of corner-connected domains, such as the row outlined in Fig. 8(*a*). However, no ordering was assumed between adjacent diagonal rows containing the same column orientation, *i.e.* the ordering of thorium atoms *along* the columns was confined to single domains.

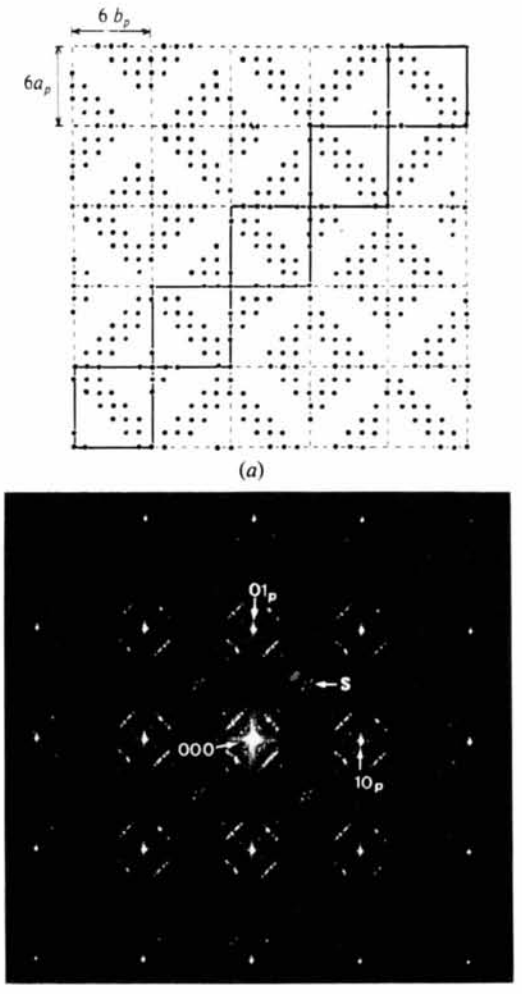

Fig. 8. (*a*) Part of the optical diffraction screen corresponding to a microdomain model for thorium/vacancy ordering in slow-cooled $ThNb_4O_{12}$. Only the thorium-atom positions were used. Dashed lines have been added to indicate the domain boundaries. The boundaries surrounding a diagonal row of corner-shared domains are emphasized by heavy lines. Note that the periodicity of alternate columns of thorium atoms and vacancies is maintained along these rows and all equivalent parallel rows. (*b*) The corresponding optical diffraction pattern. Third-order satellites are indicated by *s*.

The DP generated from this model is shown in Fig. 8(*b*). It reproduces in projection the four observed diffuse rods about each subcell reflection, with sides parallel to $g(110)_p$ and $g(\bar{1}10)_p$ (*cf.* Fig. 3 in part I). The distance from the subcell spots to the centres of the diffuse rods is $\frac{1}{6} \times d^*(110)_p$, as experimentally observed.

In the microdomain model shown in Fig. 8(*a*), no allowance has been made for the effect of small cation displacements. We previously obtained a quantitative estimate of both niobium and thorium displacements by least-squares refinement (Alario-Franco *et al.*, 1982). They are of the order of 0·25 and 0·1 Å respectively. Our microdomain model also does not allow for the possibility of segregation or clustering of thorium atoms at the domain boundaries. As is evident from Fig. 7(*a*), the orientation relationships between tilted octahedra across the mirror-twin boundaries are different from those within the domains, and it is possible that this influences the ordering of thorium atoms at the boundaries [compare the clustering of copper atoms at antiphase boundaries in CuAu II (Jehanno, 1965)]. It is apparent that when the domain size is very small, as in $ThNb_4O_{12}$, the number of atoms occurring at domain boundaries can be a significant fraction of the total number and can influence the properties of the material. However, with the optical transform experiments, we were unable to confirm if any segregation or clustering occurred at the boundaries. As discussed in part I, the diffraction effects caused by thorium/vacancy ordering (plus atomic displacements) are extremely weak and diffuse, requiring exposure times for X-rays of hundreds of hours. The total number of measurable superlattice reflections, being limited to first-order satellites only, is small, thus severely restricting the possibility of detecting such fine details as modification of ordering at domain boundaries. However, the microdomain models shown in Figs. 7(*a*) and 8(*a*) qualitatively reproduce all of the features of the DPs for slow-cooled $ThNb_4O_{12}$, and they confirm that:

1. The domain boundaries, parallel to $(100)_p$ and $(010)_p$ and with an *average* separation of $6 \times a_p$, $6 \times b_p$, are mirror-twin planes for systems of octahedral tilts about the $[110]_p$ and $[\bar{1}10]_p$ axes in successive domains.

2. The domains containing $[110]_p$ ordered columns of thorium atoms and vacancies, and those containing $[\bar{1}10]_p$ columns, form two interpenetrating sets of corner-shared domains (*cf.* the black and white squares of a checkerboard). In either set, the ordering of columns is propagated along diagonal rows perpen-

dicular to the columns, but there is no correlation between adjacent rows.

Development of order in quenched $ThNb_4O_{12}$

It was observed that as the rate of quenching of $ThNb_4O_{12}$ was increased, the perovskite subcell c_p/a_p ratio approached closer to 1 (Table 1). This suggests that, at temperatures very close to the melting point, the average structure is cubic and probably consists of short $\langle 100\rangle_p$ chains of thorium atoms alternating with rows of vacancies, as shown in Fig. 5, and statistically oriented parallel to the three cubic axes.

The first stage in the development of order in $ThNb_4O_{12}$ is ordering of thorium atoms into alternate $(001)_p$ planes. Even for the most rapidly quenched samples, the $(h,k,\frac{l}{2})_p$, l odd, superlattice reflections resulting from this ordering are sharp and well defined; *e.g.* as shown in Fig. 1(*a*). The corresponding image in Fig. 1(*b*) shows that the $(001)_p$ fringes are actually quite irregular, displaying wave-like oscillations similar to those observed in iron-doped rutiles quenched from near their melting points (Bursill, Netherway & Grey, 1978).

In contrast to the reasonably well established order along $[001]_p$, the ordering of thorium atoms and vacancies within the (half) occupied $(001)_p$ planes is very poorly developed and consists of short segments of alternately filled and empty rows of thorium atoms along $[100]_p$ and $[010]_p$. These rows are not ordered into regular domains, but rather form an irregular tweed pattern similar to those formed by cubic and tetragonal precipitates in heterogeneous cubic alloys (Chen, Morris & Khachaturyan, 1979). The resulting electron diffraction/microscopy data are consistent with the formation of predominantly diagonal boundaries [*i.e.* parallel to $(110)_p$ and $(\bar{1}10)_p$] between the $[100]_p$ and $[010]_p$ segments of thorium/vacancy ordering (see Figs. 2*c*, 6*b* and 6*d*).

Indirect support for the type of model shown in Fig. 6(*b*) is given by the fact that this model also provides a simple mechanism for the structural changes that occur in slow-cooled $ThNb_4O_{12}$. The thorium atom arrangements that form along the diagonal boundaries in the model are similar to those that occur in the slow-cooled samples, and we propose that the boundaries act as nuclei for the formation of $[110]_p$ and $[\bar{1}10]_p$ columns of thorium atoms as the material slowly cools. The relatively small number of atom movements involved in the transformation is illustrated in Fig. 9. The atom movements are all perpendicular to the rows of thorium atoms, and they consist of 4 Å hops to adjacent cuboctahedral sites. These movements may be caused by the condensation of a soft transverse mode of vibration of the rows of thorium atoms. The circled area in Fig. 3(*a*) appears to represent the type of transformation depicted in Fig. 9. The two orientations of diagonal domain boundaries in the quenched samples, parallel to $(110)_p$ and $(\bar{1}10)_p$, act as nucleating centres for the corresponding two orientations of thorium/vacancy columns in the slow-cooled samples (Fig. 8*a*). The heterogeneous nucleation and growth of these columns must lead to a microdomain texture in which the boundaries bisect the two column orientations; *i.e.* they are parallel to $(100)_p$ and $(010)_p$.

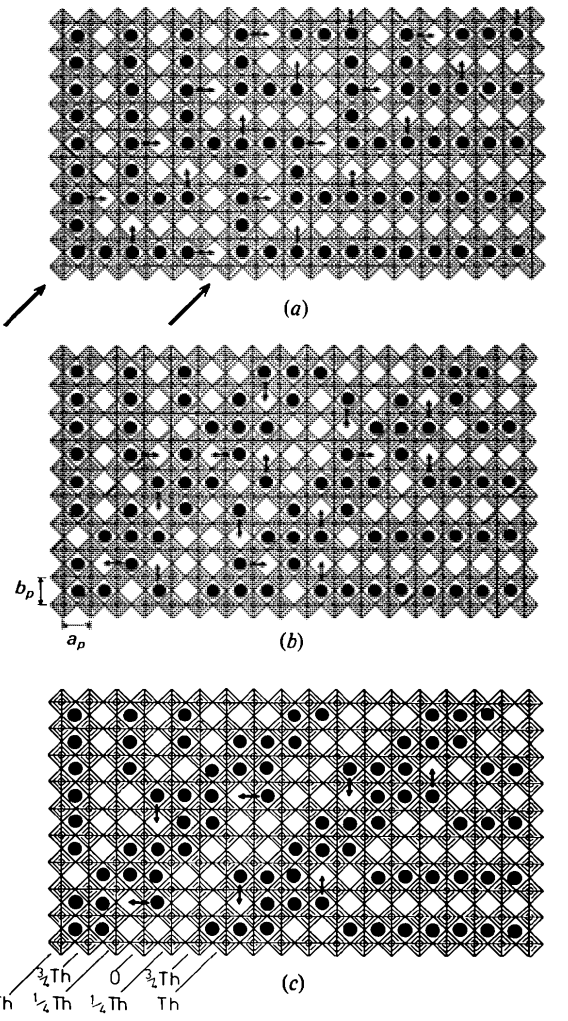

Fig. 9. Possible mechanism for the evolution of ordering with slow cooling in $ThNb_4O_{12}$. The thorium displacements necessary for the transformation from the high-temperature form (*a*) to the low-temperature form (*c*) are indicated by arrows. Thorium atoms are represented by the filled circles, $(001)_p$ section. Note in (*b*) that the average thorium occupancy of the $[110]_p$ rows (*i.e.* 0, ¼Th, ¾Th, Th, ¾Th, ¼Th, 0) corresponds to the sinusoidal modulation model reported in part I. The further thorium displacements necessary to produce an ordered alternation of three filled and three empty [110] rows is shown in (*c*). The arrows marked in (*a*) indicate domain boundaries. The ordering shown in (*b*) is a possible intermediate stage.

Many details relating to the formation of the microdomains and the structural modifications at the domain boundaries remain unknown and further studies on this interesting material are warranted, using high-resolution electron microscopy as well as inelastic neutron diffraction.

References

ALARIO-FRANCO, M. A., GREY, I. E., JOUBERT, J. C., VINCENT, H. & LABEAU, M. (1982). *Acta Cryst.* A**38**, 177–186.

BURSILL, L. A., NETHERWAY, D. J. & GREY, I. E. (1978). *Nature (London)*, **272**, 405–410.

CHEN, S., MORRIS, J. W. & KHACHATURYAN, A. G. (1979). *AIP Conf. Proc.* **53**, 168–172.

JEHANNO, G. (1965). PhD Thesis, Univ. of Paris.

KOVBA, L. M. & TRUNOV, V. K. (1962). *Dokl. Akad. Nauk SSSR*, **147**, 622–624.

LIPSON, H. (1972). *Optical Transforms*. London: Academic Press.

TRUNOV, V. K. & KOVBA, L. M. (1966). *Zh. Strukt. Khim.* **7**, 896–897.

Acta Cryst. (1982). A**38**, 761–772

Gaussian Growth-Disorder Models and Optical Transform Methods

BY T. R. WELBERRY AND C. E. CARROLL

Research School of Chemistry, Australian National University, PO Box 4, Canberra, ACT 2600, Australia

(*Received* 19 *January* 1982; *accepted* 6 *May* 1982)

Abstract

The properties of Gaussian growth-disorder models are explored and their use for producing realizations of disordered lattices for optical transform analogue experiments is described. Use of Gaussian variables provides greater flexibility than previously described binary ones and in particular enables realizations to be produced in dimensions greater than two without restriction on the values of nearest-neighbour correlation coefficients. A method of converting Gaussian realizations to binary ones is also described.

1. Introduction

Optical transform methods (Lipson, 1973) have become well established as aids in deducing the structure of materials from their X-ray diffraction patterns. Although for non-disordered single-crystal structure determination the method cannot compete with computer calculations, for non-crystalline or disordered materials the method still has considerable appeal, not least being the power of the visual presentation of results to stimulate thought and aid in the development of intuition. The production of an optical transform from a screen representing a complicated statistical distribution of atoms or molecules is just as readily performed as from one representing the simplest regular arrangement. With the advent of fast digital to film writing devices the production of the basic diffraction screen (Harburn, Miller & Welberry, 1974) is now readily performed under computer control.

However, while it is now possible to produce diffraction screens containing $\sim 10^6$ scattering points very rapidly and easily compared with the tedious manual techniques previously employed, the very size of the assembly presents quite a new problem. This concerns the way in which the actual distribution of scattering points is generated. The complicated statistical distribution of atoms and molecules mentioned above arises in nature in ways which must be mimicked in the generating computer program. While in principle the underlying physics may be understood sufficiently to make this possible, in practice the process is often far too lengthy for an assembly of points anywhere near as large as that desirable to obtain a good noise-free diffraction pattern, even for a simple physical model such as the spin-$\frac{1}{2}$ Ising model.

For this reason we have developed a number of stochastic models called 'growth-disorder models' (Welberry & Galbraith, 1973) which may be used to generate rapidly and easily, using a simple algorithm, spatial distributions of random variables having specific statistical properties. While these provide distributions less general than might be supposed to occur in real substances, they nevertheless still have considerable flexibility so that it is likely that any real physical effect may be approximated quite satisfactorily. Several examples in which these models have been used to

0567-7394/82/060761-12$01.00

BRUCE, A. D. & SCHNEIDER, T. (1977). *Phys. Rev. B*, **16**, 3991–3997.
BULOU, A., RIDOU, C., ROUSSEAU, M., NOUET, J. & HEWAT, A. (1980). *J. Phys.* **41**, 87–96.
COCHRAN, W. (1960). *Adv. Phys.* **9**, 387–423.
COWLEY, R. A. (1980). *Adv. Phys.* **29**, 1–110.
DAWSON, B., HURLEY, A. C. & MASLEN, V. W. (1967). *Proc. R. Soc. London Ser. A*, **298**, 289–306.
FUJII, Y., HOSHINO, S., YAMADA, Y. & SHIRANE, G. (1974). *Phys. Rev. B*, **9**, 4549–4559.
HUTTON, J., NELMES, R. J., MEYER, G. M. & EIRIKSSON, V. R. (1979). *J. Phys. C*, **12**, 5393–5410.
JOHNSON, C. E. (1970). *Thermal Neutron Diffraction*, edited by B. T. M. WILLIS. Oxford Univ. Press.
LANDAU, L. D. & LIFSHITZ, E. M. (1958). *Statistical Physics*. London: Pergamon.
MAIR, S. L. (1982). *J. Phys. C*, **15**, 25–36.
MAIR, S. L., BARNEA, Z., COOPER, M. J. & ROUSE, K. D. (1974). *Acta Cryst.* A**30**, 806–813.
MEGAW, H. D. (1969). *Acta Cryst.* B**25**, 1516–1517.
MEISSNER, G. & BINDER, K. (1975). *Phys. Rev. B*, **12**, 3948–3955.
POUGET, J. P., SHAPIRO, S. M. & NASSAU, K. (1979). *J. Phys. Chem. Solids*, **40**, 267–277.
ROBERTO, J. B., BATTERMAN, B. W. & KEATING, D. T. (1974). *Phys. Rev. B*, **9**, 2590–2599.
SAKATA, M., HARADA, J., COOPER, M. J. & ROUSE, K. D. (1980). *Acta Cryst.* A**36**, 7–15.
VOGT, K., PRANDL, W. & REICHARDT, W. (1981). *Z. Phys.* B**41**, 321–328.
WILLIS, B. T. M. & PRYOR, A. W. (1975). *Thermal Vibrations in Crystallography*. Cambridge Univ. Press.

Acta Cryst. (1982). A**38**, 796–799

The Fourier Transform of Actin and Other Helical Systems With Cumulative Random Angular Disorder

BY E. H. EGELMAN

Graduate Program in Biophysics, Brandeis University, Waltham, MA 02254, *USA*

AND D. J. DEROSIER

Biology Department and Rosenstiel Basic Medical Sciences Research Center, Brandeis University, Waltham, MA 02254, *USA*

(*Received* 15 *February* 1982; *accepted* 11 *May* 1982)

Abstract

A general class of helical disorder exists which can be described by cumulative random angular motions of subunits. This disorder affects layer-line intensities and widths by a factor proportional to n^2, the square of the order of the layer line. The result explains several features of actin and polytetrafluoroethylene (Teflon) transforms, and may be relevant to other helical systems.

We have described the angular motions of subunits in the F-actin helix (Egelman, Francis & DeRosier, 1982) based upon image analysis of electron micrographs. In this paper we will present an analytic treatment of the effect of this form of disorder on the transform of such a structure. Because this treatment appears to explain features of other disordered systems (such as Teflon above the 292 K transition), we believe that it may be applicable to many helical structures.

Whereas the subunit positions in an ideal helix can be described by

$$r_j = r_0$$
$$z_j = j\,\Delta z$$
$$\psi_j = \psi_{j-1} + \Delta\psi = j\,\Delta\psi,$$

we will deal with a particular form of disordered helix where subunit positions are described by

$$r_j = r_0$$
$$z_j = j\,\Delta z$$
$$\psi_j = \psi_{j-1} + \Delta\psi + \delta_j = j\,\Delta\psi + \sum_{k=1}^{j} \delta_k. \qquad (1)$$

Fig. 1 shows a model of a helix described by these equations, and Table 1 contains the first ten values of δ_j for one of the filaments in Fig. 1.

The recursive relation in (1) is nothing more than a correlated random walk in ψ, and can be parameterized in terms of the first moment and the square root of the second moment of the distribution of δ_j's:

$$\langle\delta_j\rangle; \quad \langle\delta_j^2\rangle^{1/2} = \delta_{\text{r.m.s.}}.$$

0567-7394/82/060796-04$01.00

We will define $\langle \delta_j \rangle \equiv 0$.

Thus, for a given ψ_j, we will expect to find $\psi_{j+1} = \psi_j + \Delta\psi \pm \delta_{\text{r.m.s.}}$, $\psi_{j+2} = \psi_j + 2\Delta\psi \pm 2^{1/2}\delta_{\text{r.m.s.}}$; *etc.* When $\delta_{\text{r.m.s.}}$ is small with respect to $\Delta\psi$, angular correlation will be maintained over many subunits. As $\delta_{\text{r.m.s.}}$ grows with respect to $\Delta\psi$, the correlation length will obviously fall.

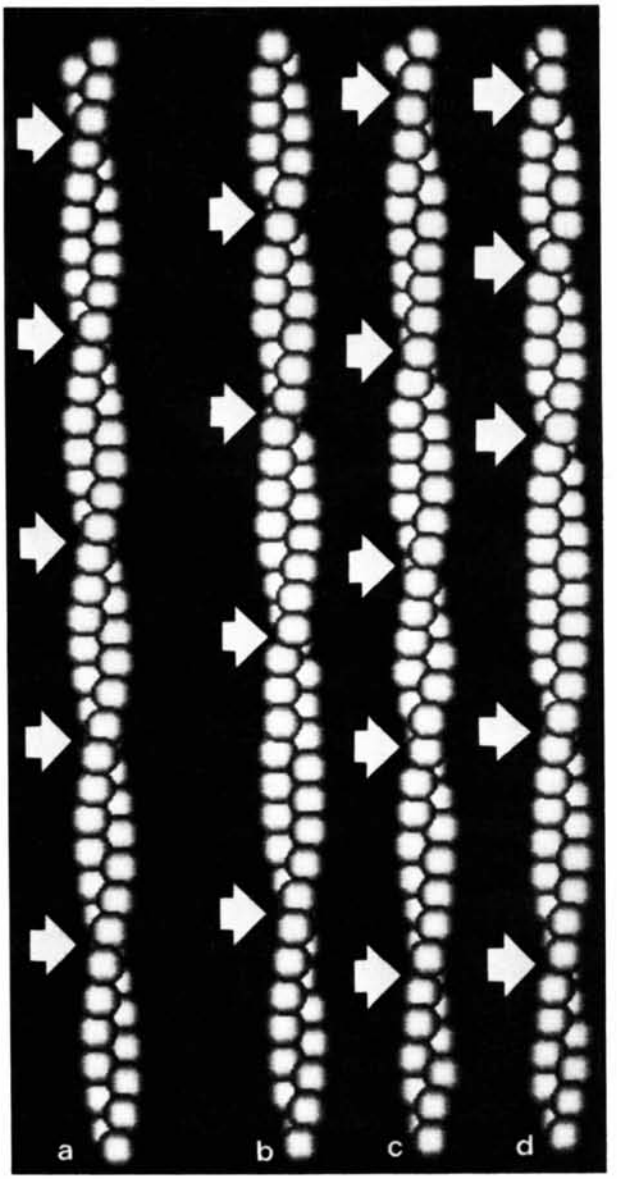

Fig. 1. A computer-generated model shows how cumulative angular disorder affects the appearance of a helical fiber. Spheres have been arranged according to the helical geometry of actin (approximately 13 subunits in six turns of a left-handed 59 Å pitch helix). In (*a*), the placement of subunits is regular. In (*b*)–(*d*), the angular rotation between subunits has an r.m.s. fluctuation of 10°, and these fluctuations have a Gaussian distribution. In all filaments shown, the axial rise per subunit is fixed, and all four filaments begin at the bottom with their first subunit in the same angular position. Because the deviations of the subunit angular positions are cumulative, the points where the right-handed two-start helices cross over (marked by the arrows) have been almost randomized in (*b*)–(*d*).

The transform of both a perfect helix and our disordered helix can be understood in terms of a product of the transform of an individual subunit multiplied by the transform of the helical lattice. In deriving the Fourier transform of the disordered helix, we can ignore the radial component, since this disorder will not affect it. The transform of the remaining axial and azimuthal components of the helix generates a sampling function $C(n,Z)$ which gives rise to layer lines. Any given layer line will have an order n associated with it which is related to the azimuthal symmetry of the corresponding helix ($n = 1$ for a one-start, $n = 2$ for a two-start, *etc.*). We will calculate this sampling function and follow the standard convention where $Z = l/c$; l = layer-line number, c = helical repeat. For the ideal helix, we have

$$C(n,Z) = \sum_{j=1}^{N} \exp|i(-n\psi_j + 2\pi Z z_j)| \tag{2}$$

using

$$\psi_j = j\,\Delta\psi$$

$$z_j = j\,\Delta z = j\,p\Delta\psi/2\pi,$$

where p is the pitch of a one-start helix,

$$C(n,Z) = \sum_{j=1}^{N} \exp|\,i(-nj\Delta\psi + jZp\Delta\psi)|$$

$$= \sum_{j=1}^{N} \exp|\,i(j\Delta\psi(pZ - n)|.$$

The corresponding $C(n,Z)$ for the disordered helix described by (1) is

$$C(n,Z) = \sum_{j=1}^{N} \exp\left[i\left(-nj\Delta\psi - n\sum_{k=1}^{j}\delta_k + 2\pi Z z_j\right)\right]$$

$$C(n,Z) = \sum_{j=1}^{N} \exp\left[i\left(j\Delta\psi(pZ - n) - n\sum_{k=1}^{j}\delta_k\right)\right]. \tag{3}$$

The exact solution of this equation depends upon the detailed knowledge of the δ_k's, including both their individual values as well as their sequence. However, using statistical methods, we can solve for the expectation value, $\langle C(n,Z)\rangle$ in terms of another expectation value, $\langle \delta_k^2 \rangle^{1/2}$. From (2) we can see that for a given n there will exist a family of $Z_{0,n}$'s (layer lines) such that

$$\Delta\psi(pZ_{0,n} - n) = 2\pi m; \quad m = 0, \pm 1, \pm 2, \ldots.$$

It can easily be shown that the disorder term in (3) will not shift the expectation value of these $Z_{0,n}$'s. This follows from the expectation value of the sum over the δ_k's being equal to zero. Therefore, the expectation value for the layer-line peak will always be at the same position it would be in the absence of disorder.

Thus, at the expected layer-line peaks, (3) reduces to

$$C(n,Z_{0,n}) = \sum_{j=1}^{N} \exp\left[-in \sum_{k=1}^{j} \delta_k\right]. \quad (4)$$

when $\delta_{\text{r.m.s.}} = 0$, $|C(n,Z)| = N$.

For the more general situation ($\delta_{\text{r.m.s.}} \neq 0$) it is helpful to rewrite the double summation in (4) as a single sum:

$$C(n,Z_{0,n}) = \sum_{j=1}^{N} \exp(-i\beta_j), \quad (5)$$

where

$$\langle(\beta_j - \beta_{j+1})^2\rangle^{1/2} = n\delta_{\text{r.m.s.}}.$$

The magnitude of this summation will build as a correlated random walk. That is, for $n\delta_{\text{r.m.s.}}$ significantly less than 2π (for actin, we have experimentally determined $\delta_{\text{r.m.s.}}$ to be of the order of 10°), successive terms in the summation will involve the addition of vectors (whose angle is given by β) which are quite well correlated in angle. Thus, these terms will build as N, the number of steps. However, over many steps, the vectors will appear to be doing a random walk in the complex plane. In this limit, the summation should grow as $N^{1/2}$.

In Fig. 2, the summation of (5) is performed for the first ten subunits of Fig. 1, filament *b*. One can see that for $n = 3$ the correlation between steps in the complex plane begins to die off much more rapidly than for $n = 1$. While both curves ($n = 1$ and $n = 3$) have a random component in their growth, it can be seen that for $N = 10$ there is still a strong correlation in both between the first step and the tenth. This description of a correlated random walk is isomorphic with the expected end-to-end distance of a long filamentous polymer, which is bending in solution. Over a very long length the filament behaves as a random coil, while over short stretches the filament is best approximated as a relatively rigid rod. The mean squared end-to-end distance of such a flexible polymer can be written as (Landau & Lifschitz, 1958)

Table 1. *Model values for cumulative disorder*

j	δ_j (°)	β_j ($n = 1$) (°)	β_j ($n = 3$) (°)
1	12·5	12·5	37·4
2	15·8	28·3	84·8
3	−15·4	12·9	38·6
4	−4·9	7·9	23·8
5	−7·8	0·1	0·4
6	6·3	6·4	19·2
7	−9·9	−3·5	−10·6
8	7·6	4·0	12·1
9	6·6	10·6	31·8
10	2·6	13·2	39·5

These are the values of δ_j for the first ten subunits of Fig. 1, filament *b*. The corresponding β_j's are as defined in equation (5).

$$\langle R^2\rangle = 2b^2\left(\frac{L}{b} - 1 + e^{-L/b}\right),$$

where b is a correlation length and L is the contour length along the polymer. The expectation value of $|C(n,Z_{0,n})|^2$ will behave in the same manner as $\langle R^2\rangle$, and we can therefore write

$$\langle|C(n,Z_{0,n})|^2\rangle = \frac{a^2}{2}\left(\frac{2N}{a} - 1 + e^{-2N/a}\right), \quad (6)$$

where N is the number of subunits (analogous to L). We have redefined the bending correlation length b in terms of a diffraction correlation length a, $2b = a$, for later simplicity. We can define this new correlation length by once again referring to polymer bending, in which we find the relationship (Landau & Lifshitz, 1958)

$$e^{-L/b} = \langle\cos\theta(L)\rangle,$$

where θ is the angle between tangents to a filament at two points separated by the contour length L. We can now write a corresponding equation for our walk in the complex plane:

$$\langle\cos(n\delta_k)\rangle = e^{-2N/a},$$

where the mean angular deviation after one subunit ($N = 1$) is $n\delta_{\text{r.m.s.}}$. For $n\delta_{\text{r.m.s.}} \ll 1$, we can expand this and we have

$$a = 4/n^2\,\delta^2_{\text{r.m.s.}}.$$

The most unusual feature of this equation is that the correlation length varies for different layer lines. For example, we determined that for actin $\delta_{\text{r.m.s.}} = 10°$. On the sixth layer line of actin where $n = -1$, $a_{-1} = 131$ subunits while on the first layer line, where $n = 2$, $a_2 = 33$ subunits.

It is important to note that the intensities of these layer lines will be differently affected. We can simplify

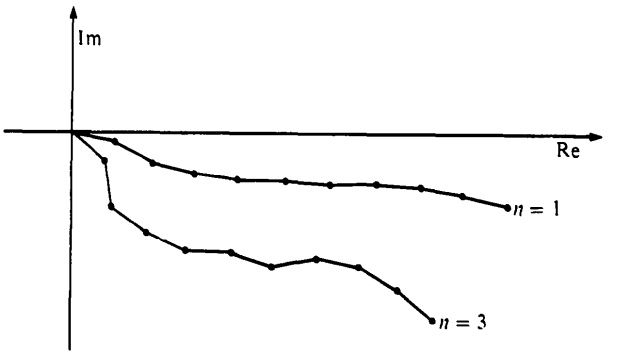

Fig. 2. The growth of the sampling function, $C(n,Z_{0,n})$, proceeds as a correlated random walk in the complex plane. We have plotted here the summation in equation (5) for the first ten subunits of Fig. 1, filament *b*. The values of δ_j and β_j for these subunits are given in Table 1.

(6) for the case where $N \gg a_n$, that is, the filaments we are diffracting from are longer than the correlation length:

$$\langle |C(n,Z_{0,n})|^2 \rangle = aN = 4N/n^2\,\delta^2_{\text{r.m.s.}}.$$

Thus, when one is dealing with lengths significantly greater than the correlation length an important feature emerges from this equation. The peak layer-line intensities (except for meridional reflections which will be unaffected by this disorder) will be weighted by a factor of $1/n^2$. Further, since the *total* intensity of scattering will still be equal to N for both the ordered and disordered case, the width of a layer line in the meridional direction will be independent of N when $N \gg a$. Since the peak intensity is equal to $4N/n^2\,\delta^2_{\text{r.m.s.}}$ the width will be equal to $n^2\,\delta^2/4$ $(= 1/a)$ in this regime. Thus the helical object diffracts as a mosaic of helical stretches of length a_n where the length is different for different layer lines.

All of these statistical predictions have been confirmed using Monte Carlo simulations of helical filaments whose geometry is described by (1). These simulations have involved up to one million subunits, and their results in terms of layer-line intensities and widths have been in excellent agreement with our analytical treatment.

The practical consequences of these features are quite significant for X-ray diffraction. As n increases, not only will the peak intensity be decreased, but the increased width of the layer line will help to make it indistinguishable from the background incoherent scatter.

We have dealt elsewhere (Egelman *et al.*, 1982) with how the predictions of this formalism successfully describe several features of the actin transform. We would like to point out here that this formalism is equally relevant for describing the unsampled fiber pattern of polytetrafluoroethylene after the 292 and 303 K transitions. It has been understood for a considerable time from X-ray diffraction (Clark & Muus, 1962*b*) and NMR (Hyndman & Origlio, 1960) that individual chains in polytetrafluoroethylene crystals undergo torsional motions after the 293 K transition and that these motions appear to be of even greater magnitude after the 303 K transition. A previous treatment (Clark & Muus, 1962*a*) of the effect of this disorder dealt only with the crystal Bragg reflections (that is, the sampled intensities on layer lines). We believe that our treatment extends this to explain the appearance of the unsampled continuous layer-line intensities arising from the disorder. Because the meridional reflections remain sharp after both of these transitions, it is reasonable to believe that our equation (1) provides a good description of the motions in the Teflon chains. The $n = 2$ $(l = 1)$ continuous peak intensity seems to disappear after the 292 K transition, while the $n = 1$ reflections on the sixth and seventh layer lines themselves weaken or disappear after the 303 K transition. This is exactly the prediction of our formalism, where the correlation length for all $n \neq 0$ falls as the temperature increases. For any given temperature, the correlation length for a layer line will be proportional to $1/n^2$.

That our equation (1) describes the disorder in Teflon fairly well is further supported by model-potential-energy calculations (DeSantis, Giglio, Liquori & Ripamonti, 1963; McMahon & McCullough, 1965; Bates, 1967; Bates & Stockmayer, 1968) for free filaments which yield a relatively shallow potential-energy well for rotations about the C–C bond. For $T = 300$ K, a shift of kT from the most stable bond angle (about 165°) appears to be equal to about ±8° (McMahon & McCullough, 1965, Fig. 2). These shifts can be mapped into the helical coordinates ψ and z. The absolute shift in $\Delta\psi$ (the angular rotation between subunits) is about the same as the shift in the bond angle, but the fractional change in $\Delta\psi$ for this amount of rotation is 15 times greater than the corresponding fractional change in the axial rise Δz of each subunit. Therefore, just like actin, almost all of the disorder is azimuthal.

Because equation (1) appears to provide a reasonable approximation of these two helical systems (actin and Teflon), it suggests that this form of disorder may be a general feature of other filamentous polymers where the number of connections between subunits is limited. The essential requirement for this formalism to be applicable is that the angular correlation for subunits must die off faster than the axial correlation. The helical structures of both actin and polytetrafluoroethylene appear to obey this requirement.

References

BATES, T. W. (1967). *Trans. Faraday Soc.* **63**, 1825.

BATES, T. W. & STOCKMAYER, W. H. (1968). *Macromolecules*, **1**, 12–24.

CLARK, E. S. & MUUS, L. T. (1962*a*). *Z. Kristallogr.* **117**, 108–118.

CLARK, E. S. & MUUS, L. T. (1962*b*). *Z. Kristallogr.* **117**, 119–127.

DESANTIS, P., GIGLIO, E., LIQUORI, A. M. & RIPAMONTI, A. (1963). *J. Polym. Sci. Part A*, **1**, 1383–1404.

EGELMAN, E. H., FRANCIS, N. & DEROSIER, D. J. (1982). *Nature (London)*, **298**, 131–135.

HYNDMAN, D. & ORIGLIO, G. F. (1960). *J. Appl. Phys.* **31**, 1849–1852.

LANDAU, L. & LIFSHITZ, E. M. (1958). *Statistical Physics*, pp. 479–482. London: Pergamon.

MCMAHON, P. E. & MCCULLOUGH, R. L. (1965). *Trans. Faraday Soc.* **61**, 201–206.